HHS Public Access

Author manuscript

IEEE Trans Biomed Eng. Author manuscript; available in PMC 2023 November 01.

Published in final edited form as:

IEEE Trans Biomed Eng. 2022 November ; 69(11): 3334–3344. doi:10.1109/TBME.2022.3168402.

Towards patient-specific optimization of neoadjuvant treatment protocols for breast cancer based on image-guided fluid dynamics

Chengyue Wu[*],
Oden Institute for Computational Engineering and Sciences, the University of Texas at Austin, Austin TX 78712 USA

David A. Hormuth II,
Oden Institute for Computational Engineering and Sciences, and Livestrong Cancer Institutes, The University of Texas at Austin, USA.

Guillermo Lorenzo,
Oden Institute for Computational Engineering and Sciences, the University of Texas at Austin; Department of Civil Engineering and Architecture, University of Pavia, Italy.

Angela M. Jarrett,
Oden Institute for Computational Engineering and Sciences, and Livestrong Cancer Institutes, The University of Texas at Austin, USA.

Federico Pineda,
Department of Radiology, The University of Chicago, USA.

Frederick M. Howard,
Section of Hematology/Oncology - Department of Medicine, The University of Chicago, USA.

Gregory S. Karczmar,
Department of Radiology, The University of Chicago, USA.

Thomas E. Yankeelov
Department of Biomedical Engineering, Department of Diagnostic Medicine, Department of Oncology, Oden Institute for Computational Engineering and Sciences, and Livestrong Cancer Institutes, The University of Texas at Austin; Department of Imaging Physics, MD Anderson Cancer Center, USA.

Abstract

Objective: This study establishes a fluid dynamics model personalized with patient-specific imaging data to optimize neoadjuvant therapy (i.e., doxorubicin) protocols for breast cancers.

Methods: Ten patients recruited at the University of Chicago were included in this study. Quantitative dynamic contrast-enhanced and diffusion weighted magnetic resonance imaging data are leveraged to estimate patient-specific hemodynamic properties, which are then used to constrain the mechanism-based drug delivery model. Then, computer simulations of this model

[*]corresponding author, cw35926@utexas.edu.

yield the subsequent drug distribution throughout the breast. By systematically varying the dosing schedule, we identify an optimized regimen for each patient using the maximum safe therapeutic duration (*MSTD*), which is a metric balancing treatment efficacy and toxicity.

Results: With an individually optimized dose (range = 12.11 – 15.11 mg/m^2 per injection), a 3-week regimen consisting of a uniform daily injection significantly outperforms all other scheduling strategies ($P < 0.001$). In particular, the optimal protocol is predicted to significantly outperform the standard protocol ($P < 0.001$), improving the *MSTD* by an average factor of 9.93 (range = 6.63 to 14.17).

Conclusion: A clinical-mathematical framework was developed by integrating quantitative MRI data, advanced image processing, and computational fluid dynamics to predict the efficacy and toxicity of neoadjuvant therapy protocols, thus enabling the rational identification of an optimal therapeutic regimen on a patient-specific basis.

Significance: Our clinical-computational approach has the potential to enable optimization of therapeutic regimens on a patient-specific basis and provide guidance for prospective clinical trials aimed at refining neoadjuvant therapy protocols for breast cancers.

Keywords

Drug delivery; Magnetic resonance imaging; Mathematical oncology; Optimal control problem; Data-driven; Clinical-computational framework

I. Introduction

Neoadjuvant therapy (NAT), which generally refers to the therapy (e.g., chemotherapy, hormone therapy, radiation therapy) administered before surgery, has become the standard-of-care for the treatment of locally advanced breast cancers [1]. NAT often results in a reduction of tumor burden, which increases the feasibility of breast conserving surgery and decreases the risk of recurrence [1,2]. However, current NAT regimens are not without limitations. Based on a recent pooled analysis of 52 studies from 1999 to 2016 [3], the pathologic complete response rate of breast cancer patients receiving NAT is highest in HER2+ tumors with a median of 50%, followed by triple-negative breast cancer (TNBC) at 32.6%, and lowest for HR+/HER2− tumors at 9.3%. Thus, there is still a substantial proportion of breast cancer patients who have suboptimal responses to standard NAT regimens. One major barrier to improving patients' response to NAT is the challenge of tailoring treatments for individual patients.

Determining which treatments are appropriate for a given breast cancer patient, as well as the dose, timing, combination, and order of those therapies, is a complex and challenging process. In the standard-of-care setting, NAT generally consists of multiple cycles of cytotoxic therapies administered every 2-4 weeks. Depending on the subtype and stage, different regimens are recommended. For example, in HER2+ disease, HER2-targeted therapies are administered in combination with chemotherapy [4,5]. In TNBC, standard NAT consists of taxane- and anthracycline-based chemotherapy [6,7]. Additionally, within each treatment cycle of a particular therapy, there is an opportunity to improve chemotherapy dosing schedules for early breast cancer [8-12]. The pivotal Intergroup

Trial C7941 demonstrated that a dose-dense (every 2 week) schedule of doxorubicin, cyclophosphamide, and paclitaxel prolonged disease-free survival when compared to the standard (every 3 week) dosing interval [11]. Subsequently, the randomized phase III E1199 trial demonstrated that weekly administration of paclitaxel resulted in superior disease free and overall survival compared to the standard three-week dosing interval, with similar rates of serious adverse events but higher incidence of neuropathy with weekly treatment [9]. Over thirty trials have examined the impact of dose intensity on disease recurrence, with a patient-level meta-analysis demonstrating a consistent benefit with shortened treatment intervals [12].

Although clinical trials provide convincing evidence of the increased efficacy of dose-dense treatment, they require thousands of patients to achieve adequate power and reach a convincing conclusion. Furthermore, each clinical trial can only investigate a very limited number of alternative therapeutic regimens. Moreover, population-based approaches cannot capture the unique biological features characterizing the tumors of individual patients, leading to sub-optimal outcomes. But given the enormous number of therapeutic options, which continuously increase as new therapeutic targets and approaches identified [5,13-15], it is simply impossible for clinical trials to experimentally evaluate all the possible drug combinations, dosing, and scheduling strategies that might be appropriate for a particular patient. Alternatively, clinical-computational approaches rely on mathematical models that can be initialized and constrained by patient-specific features to render personalized computer simulations that predict therapeutic efficacy [16]. These technologies enable the exhaustive exploration of multiple regimens *in silico*, and are therefore highly coveted as a strategy to guide treatment optimization for individual patients.

In this contribution, we present a rigorous, but practical, framework for integrating clinically available imaging data with a mechanism-based, biophysical model to predict treatment efficacy and toxicity which can then be used to optimize NAT (Fig. 1). Specifically, we use pre-treatment quantitative magnetic resonance imaging (MRI) to identify patient-specific tissue geometry and properties to personalize a computational fluid dynamic model. With this clinical-computational system, a patient-specific “digital twin” [17] is established to provide a rigorous estimate of hemodynamics and pharmacokinetics. We then systematically test in silico a large range of practical therapeutic protocols. Finally, based on an objective function which simultaneously accounts for the treatment efficacy within the tumor and the toxicity outside the tumor, the optimization of therapeutic protocols is performed for each individual patient. We test the proposed methodology in an initial set of ten breast cancer patients to identify treatment regimens designed to outperform the standard-of-care regimen. We conclude that the proposed framework has the potential to serve as a foundation for designing patient-specific therapeutic regimens that can achieve superior patient outcomes with lower toxicities.

II. Materials and Methods

A. Patient Recruitment

Ten women were enrolled in an ongoing IRB-approved study to receive a research MRI prior to biopsy (Protocols # IRB15-1596, IRB16-0396, IRB16-1410, 9127-CR012,

approved by BSD IRB Committee B, The University of Chicago Biological Sciences Division/University of Chicago Medical Center). All the patients had BI-RADS (Breast Imaging Reporting and Data System) 4 or 5 lesions identified on screening mammography. All the patients had biopsy-proved malignant breast tumors (invasive ductal carcinomas, invasive ductal carcinomas, or ductal carcinoma *in situ*). For each biopsied tumor, immunohistochemical (IHC) stains were performed to examine ER/PR reactivity, and fluorescence *in situ* hybridization or IHC staining was performed to test HER2 expression in cases of invasive cancer. Multiple subtypes of breast cancer were identified among these patients, including ER+/PR+/HER−, ER+/PR+, and TNBC (see Supplementary Table S1).

B. Therapeutic Regimens

The therapeutic regimens administered to each patient varied according to disease subtype and are summarized in Supplementary Table S1. Specifically, four of the patients underwent neoadjuvant treatment, while the other six patients received upfront surgery. We acknowledge that the heterogeneity of this patient cohort could lead to a mismatch between the simulated and administered treatments, thus the main purpose of this analysis is not to compare predicted and observed results. Rather, our objective is to develop a robust methodology that is capable of handling data types available in the clinical setting and to simulate realistic drug efficacy and toxicity effects on individual patients. Therefore, we simulate treatment with single-agent doxorubicin, an anthracycline chemotherapy that kills cancer cells *via* DNA damage [18], as it is commonly used to treat breast cancer and exhibits a narrow therapeutic index [18,19]. The methodology can be generalized to estimate performance of other therapeutic regimens including one or multiple drugs, and can also be applied to more homogeneous cohorts.

C. MRI Acquisition and Analysis

MRI studies for all enrolled patients were performed on 3T MR systems equipped with 16-channel bilateral breast coils. The scanning protocol majorly consisted of pre-constrast T_1 mapping, diffusion-weighted (DW-) MRI, and dynamic contrast-enhanced (DCE-) MRI. Detailed imaging parameters can be found in Supplementary Section S1.1. The MR images for each patient were passed through a processing pipeline [20,21] to yield tissue geometry and physiological properties. Particularly, breast contours and tissues were segmented *via* the *k*-means algorithm, vasculature was segmented *via* a Hessian-based filter, and the tumors were segmented *via* a fuzzy-c means algorithm [21]. DCE-MRI data were analyzed by a Patlak model [22] to estimate the parametric maps of the bolus arrival time (BAT), volume transfer coefficient (K^{trans}), and plasma volume fraction (v_p). BAT was used to determine blood flow directions in the vascular network, v_p used to correct radius (R) of segmented vasculature, and K^{trans} used to calibrate spatially resolved maps of vascular hydraulic conductivity (L_p) and permeability (P) *via* linear scaling [20]. DW-MRI data were analyzed by standard methods [23] to yield parametric maps of the apparent diffusion coefficient (ADC), which were then used to calibrate the spatially resolved maps of interstitial tissue hydraulic conductivity (κ) and diffusivity of small molecules (D) *via* linear scaling [20]. Supplementary Section S1.2 provides details on the calculation of parameters.

D. Image-Guided Modeling

We established a computational fluid dynamic model to describe the steady-state hemodynamics and time-dependent drug delivery over the patient's breast. The hemodynamic problem has been reported previously [20]. Briefly, the breast domain was divided into the vascular and interstitial space based on the image segmentations to model blood and interstitial flow, respectively (see Fig. 1). In the vascular space, we defined the vessel network along its centerlines and computed blood flow by solving a pseudo-1D problem *via* Poiseuille's law [24] (equation (1)), which assumes laminar blood flow through the vasculature. In the interstitial space, the flow problem was defined in 3D and governed by Darcy's law [24] (equation (2)), which states that the interstitial flow velocity is proportional to the pressure gradient and tissue hydraulic conductivity. The interaction (i.e., extravasation and re-absorption) between blood flow and interstitial flow was characterized by Starling's law [24] (equation (3)), which specifies that the extraction of fluid from intravascular to extravascular space is proportional to the pressure difference across the vessel wall and the hydraulic conductivity of the vessel wall. Thus, the steady-state hemodynamics model reads as,

$$Q_v = -\frac{\pi R^4}{8\mu}\frac{dp_v}{dl}, \quad l \in \Lambda \tag{1}$$

$$\boldsymbol{u}_t = -\kappa \nabla p_t, \quad \boldsymbol{x} \in \Omega_{\mathrm{t}} \tag{2}$$

$$q_e = Lp(p_v - p_t), \quad l \in \Lambda, \boldsymbol{x} \in \partial\Omega_{\mathrm{t}} \cap \partial\Omega_{\mathrm{v}}\,. \tag{3}$$

Detailed definitions of the geometry, variables, and parameters are provided in Table I. In the 3D tissue domain, Dirichlet boundary condition for pressure (i.e., $p_t = 2 \times 10^4$ g cm^{-1} s^{-2}) was assigned on the surface contour of breast and the chest wall, and Neumann boundary condition represented by equation (3) was assigned on the interface of the vascular and extravascular space. In the 1D vascular domain, Dirichlet boundary conditions for pressure were assigned at the terminal ends of the vascular network, where the values of terminal pressure as well as blood flow direction automatically determined using an optimization procedure informed by *BAT* measurement. Details of boundary condition determination in the vascular domain were presented in ref. 20.

To model drug delivery, we first assume that the drug propagates through the vasculature as determined by the patient's hemodynamic analysis described in the previous paragraph, and we define a source flux ($\boldsymbol{J}$; defined in equation (5)) to model interstitial drug distribution once it extravasates. The concentration of delivered drug in the interstitial domain (C_t) was then governed by the advection-diffusion equation:

$$\frac{\partial C_t}{\partial t} = -\boldsymbol{u}_t \cdot \nabla C_t + \nabla \cdot (D \nabla C_t), \quad \boldsymbol{x} \in \Omega_{\mathrm{t}} \tag{4}$$

with the drug source flux given as a boundary condition,

$$\boldsymbol{J} = P(C_p - C_t)\boldsymbol{n},\ \boldsymbol{x} \in \partial\Omega_t \cap \partial\Omega_v\ . \tag{5}$$

In addition, a no-flux boundary condition was given in the rest of breast boundary. The first term on the right-hand-side of equation (4) describes the advection of the drug carried by the bulk interstitial flow, the second term models the diffusion of drug due to a concentration gradient, and the last term represents the drug source delivered by the vasculature. The advection flow in the interstitial space was imported from the output of the hemodynamic model.

For both the hemodynamic and drug delivery components of the model, the parts regarding 1D vascular domain are spatially discretized using the finite difference method, and 3D tissue domain using the finite element method. Time stepping for the drug delivery component is represented by the Crank-Nicolson method. Detailed numerical methods can be found in Supplementary Sections 1.3 and 1.4.

Initial condition of C_t was assigned as being 0 everywhere in the breast at $t = 0$. Initial condition of C_p was determined based on the reported pharmacokinetics of doxorubicin in humans. Specifically, a single infusion of doxorubicin with a standard dose of 60 mg/m^2 body surface area (BSA) would yield a peak plasma concentration of 1 – 10 μg/ml (the average value is approximately 4.0 μg/ml), and a terminal plasma half-life of 20 – 48 h [25-27]. Therefore, we modeled the input profile of plasma concentration resulting from a single injection of a 60 mg/m^2 dose with a bi-exponential infusion-decay equation (see Supplementary Section S1.5 for details). As the administered dose changes, the magnitude of the plasma drug concentration is assumed to change proportionally. For schedules involving multiple injections, the plasma concentration profiles are determined by summing a series of one-injection-profiles scaled by the dose and appropriately delayed in time (Supplementary Figs. S3-S4).

E. Definition of the Candidate Treatment Protocols

We attempted to optimize the treatment protocol along both the scheduling and dosing dimensions. For each patient, we evaluated 14 different scheduling strategies with the same total dose within one treatment cycle lasting 3 weeks (Table II). We assumed the drug could be administered *via* a single injection of the total dose on the first day (i.e., schedule A), *via* two 1/2-dose injections on two different days (i.e., schedules B1 – B5), *via* three 1/3-dose injections on three different days (i.e., schedules C1 – C4), *via* four 1/4-dose injections on four different days (i.e., schedules D1 – D3), or *via* twenty-one 1/21-dose injections every day during the cycle (i.e., schedule E). Additionally, we tested varying the total dose administered over the range 0 – 500 mg/m^2 BSA. This range is determined from reports indicating an increased risk of clinical cardiotoxicity resulting from a cumulative dose of doxorubicin above 550 mg/m^2 BSA [19].

F. Optimization of treatment efficacy and toxicity

In computational science, optimal control aims to determine the solution of a dynamic system that achieves a desired performance over time by adequately adjusting the controls

with certain constraints [22]. In this study, the task of finding the best treatment protocol for each patient can be treated as an optimal control problem by considering the therapeutic protocols as the target control.

Towards this end, we seek to define a measure to quantify the therapeutic response of each treatment protocol estimated by the proposed model. Particularly, we adapted the concept of the "therapeutic window" which refers to the range of drug concentration that can simultaneously achieve both high efficacy and low toxicity [28]. For a specific therapy, the lower bound of the therapeutic window is set by the minimum concentration that can effectively kill cancer cells and is determined by the drug concentration inhibiting proliferation of the cells by 50% (ID_{50}). Similarly, the upper bound of the therapeutic window is set by the minimum concentration that can cause severe toxicity to healthy tissue and is determined by the drug concentration that can effectively kill 50% of healthy cells (LD_{50}). In this study, we prescribed the ID_{50} and LD_{50} as global parameters, whose values were determined by in vitro assays reported in the literature; ID_{50} = 0.25 μg/ml tissue and LD_{50} = 0.90 μg/ml for doxorubicin. Details about the determination of ID_{50} and LD_{50}, and the discussion on associated limitation, can be found in Supplementary Section S1.6. Given the ID_{50} and LD_{50}, we calculate two metrics for each concentration time course: the effective duration ($ED(\boldsymbol{x})$) and the toxic duration ($TD(\boldsymbol{x})$). The $ED(\boldsymbol{x})$ and $TD(\boldsymbol{x})$ refer to the total time that the drug concentration at location x is greater than the ID_{50} and LD_{50}, respectively. Illustrations for the calculation of therapeutic window, *ED*, and *TD* can be found in Supplementary Section S1.7 and Fig. S5.

These definitions allowed for construction of a desired measure of therapeutic response, maximum safe therapeutic duration (*MSTD*). Specifically, for each tested protocol p,

$$MSTD(p) = \frac{\int_{\Omega_{\text{tumor}}} ED(\boldsymbol{x})d\boldsymbol{x}}{\int_{\Omega_{\text{tumor}}} d\boldsymbol{x}} - \frac{\int_{\Omega_{\text{non}}} TD(\boldsymbol{x})d\boldsymbol{x}}{\int_{\Omega_{\text{non}}} d\boldsymbol{x}}, \tag{6}$$

where Ω_{tumor} refer to the tumor, and $\Omega_{\text{non}} = \Omega_t \setminus \Omega_{\text{tumor}}$ is the healthy tissue; the first term indicates the mean of $ED(\boldsymbol{x})$ within tumor, and second term indicates the mean of $TD(\boldsymbol{x})$ in the healthy tissue. Therefore, the definition of *MSTD* balances the treatment efficacy on tumor cells with the toxicity on healthy tissue. Additionally, to evaluate the improvement of the alternative protocols over the standard protocol with respect to therapeutic efficacy and safety, we defined the benefit ratio (*BR*). Specifically, for each tested protocol *p, BR* is defined as,

$$BR(p) = MSTD(p) \ / \ MSTD_0, \tag{7}$$

where $MSTD(p)$ refers to the *MSTD* obtained by the tested protocol *p*; $MSTD_0$ refers to *MSTD* obtained by the standard protocol (i.e., a dose of 60 mg/m^2 BSA *via* a single intravenous injection per 3-week cycle). In summary, the *MSTD* measures the performance of each treatment protocol by explicitly accounting for both treatment efficacy and toxicity, while the *BR* quantifies the improvement of each alternative treatment protocol relative to that of the standard treatment.

The *MSTD* is used as the objective function, and the problem can be solved as a two-step optimization scheme with the constraints determined by the practical range of schedules and doses. First, for each patient and each treatment schedule, we use a particle swarm method [29] to find the optimal total dose within the considered range. The goal was to find the dose that achieved the maximal *MSTD* under each schedule; if the dose leading to the maximal *MSTD* was a range instead of a unique number, the minimal dose in the optimized range was selected. Second, for each patient, we compared the maximal *MSTDs* obtained by all investigated schedules and identified the schedule that achieved the highest *MSTD*. Thus, this procedure results in an optimal schedule along with its corresponding optimal total dose.

III. Results

A. Patient-Specific Treatment Optimization

With maximization of the *MSTD*, we identify the optimal treatment protocol for each patient within the selected set of dosing-schedule options (Table II). Figure 2 presents the *BR* as a function of treatment schedule and total dose for each patient. Overall, assuming both schedule and total dose can be adjusted, schedule E is the optimal therapeutic schedule for all ten patients, while the associated total doses vary across patients, with a range from 270.69 to 317.28 mg/m^2 BSA. The optimal protocols show a large improvement relative to the standard protocol, which reveal *BR* from 6.63 to 14.17 among the cohort. (See Supplemental Table S2 detailed reports). These results clearly indicate that optimization of the treatment protocols can have a large effect on the *BR*, and this effect is different for each patient.

Figure 3 presents the statistical comparisons of treatment protocols among the patient cohort. Overall, the optimized protocols significantly ($P < 0.001$) increase the *MSTDs* as compared to the standard protocol (Fig. 3a). More detailly, comparing the *MSTD* achieved by each schedule with the standard and the individually optimized total dose (Fig. 3b), we notice that optimizing the total dose significantly improves the *MSTD* ($P < 0.05$) for schedules B3 – B5, C2 – C4, D1 – D3, and E. Additionally, comparing the red boxes for schedules B1 – B5 in Fig. 3b, i.e., the two-injection schedules with the individually optimized total dose, treatment protocols with an interval between injections of longer than 3 days (B2 – B5) render a significantly better therapeutic performance ($P < 0.001$) than the treatment schedule with an injection interval of 1 day (B1); while treatment protocols with injection intervals longer than 3 days (B2 – B5) are not significantly different from each other. Similarly, comparing the red boxes for schedules C1 – C4, i.e., three-injection schedules, those with injection intervals longer than 3 days (C2 – C4) also provide a significantly larger *MSTD* ($P < 0.001$) than the treatment schedule with an injection interval of 1 day (C1); while schedules with injection intervals longer than 3 days (h – j) are not significantly different from each other. Regarding the four-injection schedules (D1 – D3), those with injection intervals longer than 3 days (D2 – D3) are significantly better ($P < 0.001$) than the treatment schedule with an injection interval of 1 day (D1); while schedules with injection intervals longer than 3 days (D2 – D3) are not significantly different from each other. Moreover, among the schedules with injections evenly separated across the 3-week therapeutic cycle (i.e., B5, C4, D3, and E), increasing the injection frequency yields

significantly better treatment performances ($P < 0.05$; see Fig. 3b, where the red boxes show $MSTD$(E) > $MSTD$(D3) > $MSTD$(C4) > $MSTD$(B5)).

The patient-specific optimization can also be interpreted along the dimensions of schedule or dose. Given a candidate schedule, the optimized total doses have a large variation across patients (Fig. 4a). For example, with schedule A, the optimal total dose varies from 32.20 mg/m^2 (Patient 3) to 87.78 mg/m^2 (Patient 7; see also Supplemental Fig. S6). For each patient, different schedules yield different optimal total doses (Fig. 4a); optimizing a schedule with a higher injection frequency tends to require a higher total dose. For example, for Patient 1, the optimal doses for schedules A, B5, C4, and E are 38.29, 76.41, 112.03, and 280.99 mg/m^2, respectively. Therefore, assuming the total dose can be adjusted, a set of alternative schedules can be identified to provide a range of options for each patient (Fig. 4b). In particular, schedules C2, C3, C4, D2, and D3 always rank within the top five, with the associated optimized total dose varying from 92.74 to 258.94 mg/m^2 BSA, and the obtained BR varying from 2.70 to 5.42.

In contrast, given a fixed total dose, the optimal schedules can vary across patients, especially when the total dose is low (Fig 4c). For example, with a total dose of 60 mg/m^2, the optimal schedule for Patient 1 is D1, while the optimal schedule for Patient 2 is C2 (also see Supplemental Fig. S7). For each patient, different total doses yield different optimal schedules (Fig. 4c). When the total dose is smaller than 100 mg/m^2, schedules with small intervals are preferred (i.e., A, B1, C1, C2, D1, or D2); while if the total dose is larger than 180 mg/m^2, schedule E is always the optimal. Therefore, assuming schedules can be adjusted, a set of total doses can be identified to provide a range of options for each patient (Fig. 4d). Specifically, the highest BR is always achieved by a total dose within the range of 180 – 360 mg/m^2, with schedule E.

More analyses regarding the correlations between image-measured tissue properties and personally optimized treatment protocols are included in Supplemental section 2.2. These results speak to the importance of incorporating patient-specific characteristics when attempting to optimize therapy for individual patients.

B. Efficacy Assessment of the Treatment Protocols

Our analysis shows that different treatment protocols result in stark differences in therapeutic performance in terms of $MSTD$ and BR for all the injection protocols tested herein. These differences ultimately stem from large variations in $ED(\boldsymbol{x})$ and $TD(\boldsymbol{x})$ values across the patients during each of the candidate protocols. For example, for Patient 1, the standard protocol achieved an voxel-wise $ED(\boldsymbol{x})$ with median (interquartile range) of 2.50 (2.33 – 2.67) days within the tumor (Fig. 5a), and a $TD(\boldsymbol{x})$ of 1.17 (0.92 – 1.25) days in the healthy tissue (Fig. 5d); while the optimal protocol achieved an $ED(\boldsymbol{x})$ of 20.92 (20.83–20.92) days within the tumor (Fig. 5b), and a $TD(\boldsymbol{x})$ of 0.00 (0.00 – 0.00) days in the healthy tissue (Fig. 5e). Both the $ED(\boldsymbol{x})$ and $TD(\boldsymbol{x})$ are significantly different ($P < 0.001$; Fig. 5c and 5f) between the standard and optimal protocols. Similarly, for Patient 2, the standard protocol achieved an $ED(\boldsymbol{x})$ of 3.25 (3.08 – 3.42) days within the tumor (Fig. 5g), and a $TD(\boldsymbol{x})$ of 1.00 (0.00 – 1.17) days in the healthy tissue (Fig. 5j); while the optimal protocol achieved an $ED(\boldsymbol{x})$ of 20.50 (20.17 – 20.58) days within the tumor (Fig. 5h), and a $TD(\boldsymbol{x})$

of 0.00 (0.00 – 0.00) days in the healthy tissue (Fig. 5k). Again, the $ED(\boldsymbol{x})$ and $TD(\boldsymbol{x})$ are significantly different ($P < 0.001$; Fig. 5i and 5l) between the two protocols. Additionally, it is worth to notice that, under the optimized protocols, there are isolated regions surrounding the main large vessels (i.e., red spots in Fig. 5e and 5f) receiving a high load of the drug, and hence exhibit high $TD(\boldsymbol{x})$. In particular, the regions adjacent to large vessels have a $TD(\boldsymbol{x})$ of 1.58 (1.58 – 3.25) days in Patient 1, and 4.92 (3.08 – 7.00) days in Patient 2. Even though these regions constitute a small fraction of the whole tissue space and therefore have very little effect on the statistics, they might warrant special attention as indicators of potential vascular toxicity. A complete report of $ED(x)$ and $TD(\boldsymbol{x})$ maps obtained for the standard and optimized protocols for all patients can be found in Table S3 and Figs. S9a - j.

C. Dynamics of Drug Distribution

To obtain the $ED(\boldsymbol{x})$ and $TD(\boldsymbol{x})$ maps and enable the identification of the optimized injection protocol for each patient, our mechanism-based model estimates the spatiotemporal distribution of drug concentration over the patient's breast anatomy under each of the candidate treatment protocols. We observe that these spatiotemporal maps of drug concentration show large variations both across the patient cohort and the candidate treatment schedules, thereby driving the differences in $ED(\boldsymbol{x})$ and $TD(\boldsymbol{x})$ maps that ultimately underlie the variations in $MSTD$ and BR. For example, Fig. 6a-b show 3D renderings of the concentration of doxorubicin at four time points under the standard and optimal treatment schemes, respectively, for Patient 1; Fig. 6c displays the median (and range) of the time course of the concentration of doxorubicin within the tumor. In this case, the optimal treatment protocol consists of daily injections of a 13.38 mg/m^2 BSA dose across a 3-week therapeutic cycle. Observe that the standard treatment scheme yields a peak median concentration in the tumor of 1.94 μg/ml at 6 hours after injection, and the concentration drops to 6.28×10^{-3} μg/ml after one week. Conversely, the optimal treatment scheme reaches the first peak of median concentration in the tumor of 0.43 μg/ml at 6 hours after injection, but in this regimen the following doses lead to an oscillatory pattern with increasingly higher concentrations that stabilizes after the third injection to a range from 0.45 to 0.76 ug/ml. Similar renderings and plots for Patient 2 are given in Fig. 6d-f. In this case, the optimal treatment protocol consists of daily injections of a 14.88 mg/m^2 BSA dose across a 3-week therapeutic cycle. Observe that the standard treatment scheme yields a peak median concentration in the tumor of 1.11 μg/ml at 20 hours after injection, and the concentration drops to 0.03 μg/ml after one week. Conversely, the optimal treatment scheme reaches the first peak of median concentration in the tumor of 0.27 μg/ml at 20 hours after injection, but in this regimen the following doses lead to an oscillatory pattern with increasingly higher concentrations that stabilizes after the fourth injection to a range from 0.52 to 0.70 μg/ml.

The different dynamics of drug distribution between these two patients (Fig. 6c and 6f) are probably due to their unique tissue properties and associated hemodynamic environments in the constructed "digital twins". In particular, Patient 1 has an image-derived vascular permeability (i.e., P in Eq. 5) to the drug of 8.24×10^{-6} (3.80×10^{-6} – 14.50×10^{-6}) ml/(cm^2 s), and model-estimated interstitial flow velocity (i.e., $\boldsymbol{u}_t$ in Eq. 3) of 8.67×10^{-8} (2.72×10^{-8} – 21.72×10^{-8}) cm/s. (Results present as median and interquartile range.) Patient 2

has an image-derived vascular permeability to the drug of 2.96×10^{-6} (1.74×10^{-6} – 4.53×10^{-6}) ml/(cm^2 s) and model-estimated interstitial flow velocity of 4.49×10^{-8} (1.59×10^{-8} – 10.29×10^{-8}) cm/s. Comparing using Wilcoxon rank sum test, Patient 1 has a significantly higher vascular permeability ($P < 0.001$) and higher interstitial flow ($P < 0.001$) than Patient 2, which leads to a faster drug uptake and higher peak concentration, therefore a larger range of concentration oscillation in the optimized protocol. This observation indicates the importance of accounting for individual differences in hydrodynamics when estimating the drug distribution for different patients.

The 3D renderings for the remaining eight patients can be found in Supplementary Fig S10.a - S10.j. Supplementary Movies S1.a - S1.j and S2.a - S2.j display the spatiotemporal changes in drug distribution during the entire treatment cycle. Additionally, Supplementary Fig S11.a - S11.j presents the drug concentration within each tumor during the entire time course for each patient during the standard and optimal treatment protocols.

IV. Discussion

The ability of DCE-MRI and DW-MRI to provide valuable prognostic information early during NAT has been well-established [30,31,32]. These studies provide evidence that MRI-derived measures of tumor status contain information that is strongly related to eventual patient response; and provide great motivation for incorporating MRI-derived measures of tumor properties to constrain predictive models for optimizing treatment regimens for the individual patient.

In this study, we have established a practical clinical-mathematical framework to identify optimal NAT regimens by maximizing efficacy and minimizing toxicity for each patient. The framework integrates quantitative MRI, advanced image analysis, and mathematical modeling to rigorously establish a “digital twin” that can be used to test a large range of potential treatment protocols for each individual patient. Based on the results, we find that therapies administered at uniform intervals and multiple small doses are predicted to outperform the current standard-of-care protocol. This observation shows matches with the principle suggested by the dose-dense hypothesis [33-36]; namely, that minimizing the regrowth of cancer between administrations of therapy would maximize the cumulative cell kill, thereby achieving greater clinical benefit. This observation also matches the results of dose-dense clinical trials in breast cancer that were successful on improving clinical outcomes [10,11,37]. Therefore, our approach provides a reasonable way to quantify the balance between drug efficacy and toxicity.

Our results further indicate that personalizing total dose administered for each patient can magnify the benefit of treatment. Increased therapeutic efficacy can be achieved with higher injection frequency only when the corresponding optimized doses are identified. The regimens with higher injection frequency usually require a lower dose per injection (to balance toxicity concerns), but higher total dose (to sufficiently suppress tumor regrowth between injections). In fact, without individually optimized doses, many of the treatment scheduling strategies evaluated in our study would no longer improve outcomes over standard treatment. This is one possible explanation for why some clinical trials failed to

demonstrate significant differences between dose-dense and conventional regimens [38], or between different dose-dense regimens [39]. We acknowledge that it may be infeasible to administer treatment daily (i.e., E) due to the increased time commitment required from patients and staff, and limited operating hours of most infusion centers. Alternatively, scheduling strategies featuring four injections of 1/4 the total dose each with 3- or 5-day intervals (i.e., D2 – D3), or three injections of 1/3 the total dose each with 3-, 5-, or 7-day intervals (i.e., C2 – C4) may be more practical, while also providing significantly superior results compared to standard NAT (see Fig. 4).

Our results also indicate that personalizing the therapeutic schedule is important if the total dose is fixed to a small value. Specifically, when the total dose is restricted to be less than 100 mg/m^2, the optimal schedules vary across patients and depend on the specific dose. In general, smaller doses require treatment schedules with shorter injection intervals. A possible explanation of this observation is that when the total dose is small, split doses would be too weak to suppress tumor growth per injection. Rather, the small dose needs to be given within a short duration to achieve sufficient efficacy (e.g., a single-injection like A, or a multiple-injection with short time-intervals like B1, C1, or D1). In contrast, when the total dose is allowed to be larger than 180 mg/m^2, splitting the total dose into daily injections still preserves sufficient efficacy per injection, which leads to the observation that schedule E (with highest injection frequency) is always identified as the optimal for all patients in the cohort (see Fig. 4).

However, the insensitivity to schedule selection when the total dose is large may also relate to a primary limitation of our current model; namely, the current assignment of a constant ID_{50} value based on doxorubicin-sensitive cell lines. This is suboptimal and most likely does not capture the heterogeneity of the patient cohort. Future efforts are desired to characterize patient heterogeneity regarding treatment sensitivity and toxicity. Assignment of patient-specific ID_{50} and LD_{50} based on clinically available biomarkers, or calibration of patient-specific sensitivity and toxicity using longitudinally monitoring data, are potentially more realistic solutions. (See Supplemental section 1.6 for more details.)

Another strength of this study is the range of doses optimized by our system mirrors the dosing administered in clinical settings, which further supports the feasibility of this methodology. Specifically, for the schedule with a single injection (i.e., A), the optimal total doses have a median (range) of 56.52 (32.20 – 87.78) mg/m^2, which is well-aligned with the clinically suggested standard dose, 60 mg/m^2, for single administration per cycle. Similarly, the optimal total doses for schedules B1, C1, and D1 are 55.81 (41.15 – 77.08) mg/m^2, 63.40 (53.69 – 80.80) mg/m^2, and 74.52 (65.55 – 88.28) mg/m^2, respectively, which are also viable as a previous phase I study demonstrated that 20 mg/m^2 daily for a 96-hour administration is tolerable [40]. Other schedules with longer injection intervals reveal larger optimal total doses, which matches with reports supporting prolonged infusion as cardioprotective [41]. For the continuous daily administration (i.e., E), however, we recognize that even though the optimal total doses are still within a viable range, the median (range) of 291.52 (270.69 – 317.28) mg/m^2 is quite large. This could bring increasing risks of dose-dependent decline in cardiac ejection fraction, as large-scale studies [19] demonstrated that 8.8% of patients have a decline at a cumulative dose of 250 mg/m^2, and 32.4% of patients have a decline at 400

mg/m^2. Although the dose was administered *via* a single injection in these studies, instead of prolonged injections, it suggests a potential concern that our current objective function, *MSTD*, could underestimate the toxicity when the total dose is large (> 250 mg/m^2). Future efforts refining the objective function at high total dose, as well as validation with animal experiments or clinical trials, are desired.

Clinical feasibility is another essential consideration when assessing the potential of applying our optimization framework in practice. Our current approach was performed on a standard laptop (MacBook Pro with CPU: 2.7GHz Intel Core i5, Memory: 8GB 1867MHz DDR3) and without using parallel computation. This very basic implementation took approximately 9 hours to optimize the therapeutic protocols for one patient; this includes 2 h for image processing, 10 min for the steady-state hemodynamic calculation [20,21], and multiple 30 min simulations of drug distribution over a 3-week cycle for 14 candidate therapeutic schedules. Fortunately, several components in the procedure can be parallelized. Assuming access to a regular multi-core computational platform, it is possible to finish the optimization of therapeutic protocols within 1.5 hours.

A natural extension of our clinical-mathematical framework is to incorporate mechanism-based models of tumor response that describe tumor growth, invasion, proliferation, death, and the immune response [42-45]. This extension would further enable explicit modeling of tumor response to treatment and provide outputs that can be directly compared to clinical endpoints for validation (e.g., tumor volume). Furthermore, in addition to pre-treatment images, imaging measurements from subsequent time points collected during NAT provide the opportunity to recalibrate the model and, hence, dynamically update its parameters to account for treatment-induced changes in tumor biology. This strategy would ultimately enable a more accurate determination of optimal treatment protocols and, potentially, superior patient outcomes. Evolving the calibrated parameters over time will also provide new insights into changes in the underlying tumor biology during therapy [44,45].

It is also important to note that the proposed model could be refined in several ways to provide a more realistic characterization of drug delivery. For example, the vasculature employed in the model are those vessels visible given the spatial resolution limitations of MRI (i.e., radii in the range of 104 to 188 μm). Neglecting microvasculature could lead to an underestimation of local perfusion and interstitial flow, and as a result, cause a systematic bias in the estimated concentration of therapeutics. A potential way to overcome this challenge is through multi-scale modeling [46], which could couple the terminal ends or the surface of visible vasculature with lower-level vascular models of microvasculature [47-50]. Furthermore, the current model could be amended to incorporate additional biological factors contributing to the drug pharmacokinetics, such as draining of interstitial fluid and drugs through the lymphatic system, and the effect of drugs on the vasculature. However, incorporating such phenomena in the mathematical formalism would necessarily require additional (possibly invasive) measurements. Thus, while the proposed framework is somewhat simplified, it does offer a rigorous, practical starting point for quantifying drug delivery on a patient-specific basis.

V. Conclusion

A clinical-mathematical framework was developed to integrate quantitative MRI data, advanced image analyses, and established laws of fluid dynamics to predict the efficacy and toxicity of a range of NAT protocols, thus enabling the rational identification of an optimal therapeutic regimen on a patient-specific basis. We posit that such a technology also provides guidance for future, prospective clinical trials in treatment design for breast cancer and, indeed, any solid tumor for which NAT is indicated and the requisite data is accessible.

Supplementary Material

Refer to Web version on PubMed Central for supplementary material.

Acknowledgments

This work is supported by National Cancer Institute through U01CA142565, U01CA174706, U01CA253540, R01CA218700, R01CA172801, U24CA226110 and P30CA014599, and the Cancer Prevention and Research Institute of Texas through RR160005. G. Lorenzo is supported by the European Union's Horizon 2020 research and innovation programme through the Marie Skłodowska-Curie grant agreement No. 838786, We offer a sincere thank you to all the women who volunteered to participate in our studies. Your strength is a lesson for all of us.

REFERENCES

[1]. Liedtke C et al. , "Response to neoadjuvant therapy and long-term survival in patients with triple-negative breast cancer," J Clin Oncol, vol. 26, no. 8, pp. 1275–1281, 2008. [PubMed: 18250347]

[2]. Broglio KR et al. , "Association of pathologic complete response to neoadjuvant therapy in HER2-positive breast cancer with long-term outcomes: a meta-analysis," JAMA Oncol, vol. 2, no. 6, pp.751–760, 2016. [PubMed: 26914222]

[3]. Spring LM et al. , "Pathological complete response after neoadjuvant chemotherapy and impact on breast cancer recurrence and survival: a comprehensive meta-analysis," Clin Cancer Res, vol. 26, no. 12, pp. 1–11, 2020. [PubMed: 31900310]

[4]. Gianni L et al. , "Efficacy and safety of neoadjuvant pertuzumab and trastuzumab in women with locally advanced, inflammatory, or early HER2-positive breast cancer (NeoSphere): a randomised multicentre, open-label, phase 2 trial," Lancet Oncol, vol. 13, no. 1, pp. 25–32, 2012. [PubMed: 22153890]

[5]. Baselga J et al. , "Lapatinib with trastuzumab for HER2-positive early breast cancer (NeoALTTO): a randomised, open-label, multicentre, phase 3 trial," Lancet, vol. 379, no. 9816, pp. 633–640, 2012. [PubMed: 22257673]

[6]. Lee JS, Yost SE, Yuan Y. "Neoadjuvant treatment for triple negative breast cancer: Recent progresses and challenges," Cancers, vol. 12, no. 6, pp. 1404, 2020.

[7]. Fitzpatrick A, Tutt A. "Controversial issues in the neoadjuvant treatment of triple-negative breast cancer," Ther Adv Med Oncol, vol. 11, pp. 1758835919882581, 2019. [PubMed: 31700549]

[8]. Hryniuk W, Levine MN. "Analysis of dose intensity for adjuvant chemotherapy trials in stage II breast cancer," J Clin Oncol, vol. 4, no. 8, pp. 1162–1170, 1986. [PubMed: 3525765]

[9]. Sparano JA et al. , "Long-term follow-up of the E1199 phase III trial evaluating the role of taxane and schedule in operable breast cancer," J Clin Oncol, vol. 33, no. 21, pp. 2353, 2015. [PubMed: 26077235]

[10]. Reinisch M, Ataseven B, Kümmel S. "Neoadjuvant dose-dense and dose-intensified chemotherapy in breast cancer-review of the literature," Breast Care, vol. 11, no. 1, pp. 13–20, 2016. [PubMed: 27051390]

[11]. Citron ML et al. , "Randomized trial of dose-dense versus conventionally scheduled and sequential versus concurrent combination chemotherapy as postoperative adjuvant treatment of

node-positive primary breast cancer: first report of Intergroup Trial C9741/Cancer and Leukemia Group B Trial 9741," J Clin Oncol, vol. 21, no. 8, pp. 1431–1439, 2003. [PubMed: 12668651]

[12]. Gray R et al. , "Increasing the dose intensity of chemotherapy by more frequent administration or sequential scheduling: a patient-level meta-analysis of 37 298 women with early breast cancer in 26 randomised trials," Lancet vol. 393, no. 10179, pp. 1440–1452, 2019.

[13]. Lehmann BD et al. , "Identification of human triple-negative breast cancer subtypes and preclinical models for selection of targeted therapies," J Clin Invest, vol. 121, no. 7, pp. 2750–2767, 2011. [PubMed: 21633166]

[14]. Chien AJ et al. , "MK-2206 and standard neoadjuvant chemotherapy improves response in patients with human epidermal growth factor receptor 2-positive and/or hormone receptor–negative breast cancers in the I-SPY 2 trial," J Clin Oncol, vol. 38, no. 10, pp. 1059–1069, 2020. [PubMed: 32031889]

[15]. Loibl S et al. , "Neoadjuvant buparlisib plus trastuzumab and paclitaxel for women with HER2+ primary breast cancer: a randomised, double-blind, placebo-controlled phase II trial (NeoPHOEBE)," Eur J Cancer, vol. 85, pp. 133–145, 2017. [PubMed: 28923573]

[16]. Hormuth DA et al. , "Math, magnets, and medicine: enabling personalized oncology," Expert Rev Precis Med Drug Dev, vol. 6, no. 2, pp. 79–81, 2021. [PubMed: 34027102]

[17]. Bruynseels K, Santoni de Sio F, van den Hoven J. "Digital twins in health care: ethical implications of an emerging engineering paradigm," Front Genet, vol. 9, pp. 31, 2018. [PubMed: 29487613]

[18]. Blum RH, Carter SK. "Adriamycin: a new anticancer drug with significant clinical activity," Ann Intern Med, vol. 80, no. 2, pp. 249–259, 1974. [PubMed: 4590654]

[19]. Swain SM, Whaley FS, Ewer MS. "Congestive heart failure in patients treated with doxorubicin: a retrospective analysis of three trials," Cancer, vol. 97, no. 11, pp. 2869–2879, 2003. [PubMed: 12767102]

[20]. Wu C et al. , "Patient-Specific Characterization of Breast Cancer Hemodynamics Using Image-Guided Computational Fluid Dynamics," IEEE Trans Med Imaging, vol. 39, no. 9, pp. 2760–2771, 2020. [PubMed: 32086203]

[21]. Wu C et al. , "Quantitative analysis of vascular properties derived from ultrafast DCE-MRI to discriminate malignant and benign breast tumors," Magn Reson Med, vol. 81, no. 3, pp. 2147–2160, 2019. [PubMed: 30368906]

[22]. Ewing JR et al. , "Patlak plots of Gd-DTPA MRI data yield blood-brain transfer constants concordant with those of 14C-sucrose in areas of blood-brain opening," Magn Reson Med, vol. 50, no. 2, pp. 283–292, 2003. [PubMed: 12876704]

[23]. Woodhams R et al. , "Diffusion-weighted imaging of the breast: principles and clinical applications," Radiographics, vol. 31, no. 4, pp. 1059–1084, 2011. [PubMed: 21768239]

[24]. D'Angelo C, Quarteroni A. "On the coupling of 1D and 3D diffusion-reaction equations: application to tissue perfusion problems," Math Models Methods Appl Sci, vol. 18, no. 08, pp. 1481–1504, 2008.

[25]. Burridge PW et al. , "Human induced pluripotent stem cell–derived cardiomyocytes recapitulate the predilection of breast cancer patients to doxorubicin-induced cardiotoxicity," Nat Med, vol. 22, no. 5, pp. 547, 2016. [PubMed: 27089514]

[26]. Barpe DR, Rosa DD, Froehlich PE. "Pharmacokinetic evaluation of doxorubicin plasma levels in normal and overweight patients with breast cancer and simulation of dose adjustment by different indexes of body mass," Eur J Pharm Sci, vol. 41, no. 3-4, pp. 458–463, 2010. [PubMed: 20688160]

[27]. Kontny NE et al. , "Population pharmacokinetics of doxorubicin: establishment of a NONMEM model for adults and children older than 3 years," Cancer Chemother Pharmacol, vol. 71, no. 3, pp. 749–763, 2013. [PubMed: 23314734]

[28]. Goodman LS et al., Goodman & Gilman's the pharmacological basis of therapeutics. New York:McGraw-Hill, 2006.

[29]. Pedersen MEH. "Good Parameters for Particle Swarm Optimization," Tech Rep, HL1001, pp. 1551–3203, 2010.

[30]. Virostko J et al. , “Dynamic contrast-enhanced magnetic resonance imaging and diffusion-weighted magnetic resonance imaging for predicting the response of locally advanced breast cancer to neoadjuvant therapy: a meta-analysis,” J Med Imaging, vol. 5, no. 1, pp. 011011, 2017.

[31]. Marinovich ML et al. , “Early prediction of pathologic response to neoadjuvant therapy in breast cancer: systematic review of the accuracy of MRI,” The Breast, vol. 21, no. 5, pp. 669–677, 2012. [PubMed: 22863284]

[32]. Cheng Q et al. , “The diagnostic performance of DCE-MRI in evaluating the pathological response to neoadjuvant chemotherapy in breast cancer: a meta-analysis,” Front Oncol, vol. 10, pp. 93, 2020. [PubMed: 32117747]

[33]. Simon R, Norton L, “The Norton–Simon hypothesis: designing more effective and less toxic chemotherapeutic regimens,” Nat Clin Pract Oncol, vol. 3, no. 8, pp. 406–407, 2006. [PubMed: 16894366]

[34]. Norton L, “Evolving concepts in the systemic drug therapy of breast cancer,” Semin Oncol, vol. 24, no. 4 Suppl 10, pp. S10–13, 1997.

[35]. Budman DR et al. , “Dose and dose intensity as determinants of outcome in the adjuvant treatment of breast cancer,” J Natl Cancer Inst, vol. 90, no. 16, pp. 1205–1211, 1998. [PubMed: 9719081]

[36]. Citron ML, “Dose-dense chemotherapy: principles, clinical results and future perspectives,” Breast Care, vol. 3, no. 4, pp.251–255, 2008. [PubMed: 21076605]

[37]. Bonilla L et al. , “Dose-dense chemotherapy in nonmetastatic breast cancer: a systematic review and meta-analysis of randomized controlled trials,” J Natl Cancer Inst, vol. 102, no. 24, pp. 1845–1854, 2010. [PubMed: 21098761]

[38]. Ellis GK et al. , “Phase III comparison of standard doxorubicin and cyclophosphamide versus weekly doxorubicin and daily oral cyclophosphamide plus granulocyte colony-stimulating factor as neoadjuvant therapy for inflammatory and locally advanced breast cancer: SWOG 0012,” J Clin Oncol, vol. 29, no. 8, pp. 1014, 2011. [PubMed: 21220618]

[39]. Schneeweiss A et al. , “Intense dose-dense epirubicin, paclitaxel, cyclophosphamide versus weekly paclitaxel, liposomal doxorubicin (plus carboplatin in triple-negative breast cancer) for neoadjuvant treatment of high-risk early breast cancer (GeparOcto—GBG 84): A randomised phase III trial,” Eur J Cancer, vol. 106, pp. 181–192, 2019. [PubMed: 30528802]

[40]. Bugat R et al. , “Clinical and pharmacokinetic study of 96-h infusions of doxorubicin in advanced cancer patients,” Eur J Cancer Clin Oncol, vol. 25, no. 3, pp. 505–511, 1989. [PubMed: 2703005]

[41]. van Dalen EC, van der Pal HJ, Kremer LC. “Different dosage schedules for reducing cardiotoxicity in people with cancer receiving anthracycline chemotherapy,” Cochrane Database Syst Rev vol. 3, pp. CD005008, 2016. [PubMed: 26938118]

[42]. Jarrett AM et al. , “Evaluating patient-specific neoadjuvant regimens for breast cancer via a mathematical model constrained by quantitative magnetic resonance imaging data,” Neoplasia, vol. 22, no. 12, pp. 820–830, 2020. [PubMed: 33197744]

[43]. Jarrett AM et al. , “Towards integration of 64Cu-DOTA-trastuzumab PET-CT and MRI with mathematical modeling to predict response to neoadjuvant therapy in HER2+ breast cancer,” Sci Rep, vol. 10, no. 1, pp. 20518, 2020. [PubMed: 33239688]

[44]. Jarrett AM et al. , “Mathematical modelling of trastuzumab-induced immune response in an in vivo murine model of HER2+ breast cancer,” Math Med Bio, vol. 36, no. 3, pp. 381–410, 2019. [PubMed: 30239754]

[45]. Almendro V et al. , “Inference of tumor evolution during chemotherapy by computational modeling and in situ analysis of genetic and phenotypic cellular diversity,” Cell Rep, vol. 6, no. 3, pp. 514–527, 2014. [PubMed: 24462293]

[46]. Yankeelov TE et al. , “Multi-Scale Imaging to Enable Multi-Scale Modeling for Predicting Tumor Growth and Treatment Response,” Biophys J, vol. 116, no. 3, pp. 323a–324a, 2019.

[47]. Filonova V et al. , “A Multiscale Framework for Defining Homeostasis in Distal Vascular Trees: Applications to the Pulmonary Circulation,” arXiv preprint, arXiv:2001.04880, 2020.

[48]. Scianna M, Bell CG, Preziosi L. “A review of mathematical models for the formation of vascular networks,” J Theor Biol, vol. 333, pp. 174–209, 2013. [PubMed: 23684907]

[49]. Phillips CM et al. , “A hybrid model of tumor growth and angiogenesis: In silico experiments,” PLOS ONE, vol. 15, no. 4, pp. e0231137, 2020. [PubMed: 32275674]

[50]. Hormuth DA et al. , “Biologically-Based Mathematical Modeling of Tumor Vasculature and Angiogenesis via Time-Resolved Imaging Data.” Cancers vol. 13, no. 12, pp. 3008, 2021. [PubMed: 34208448]

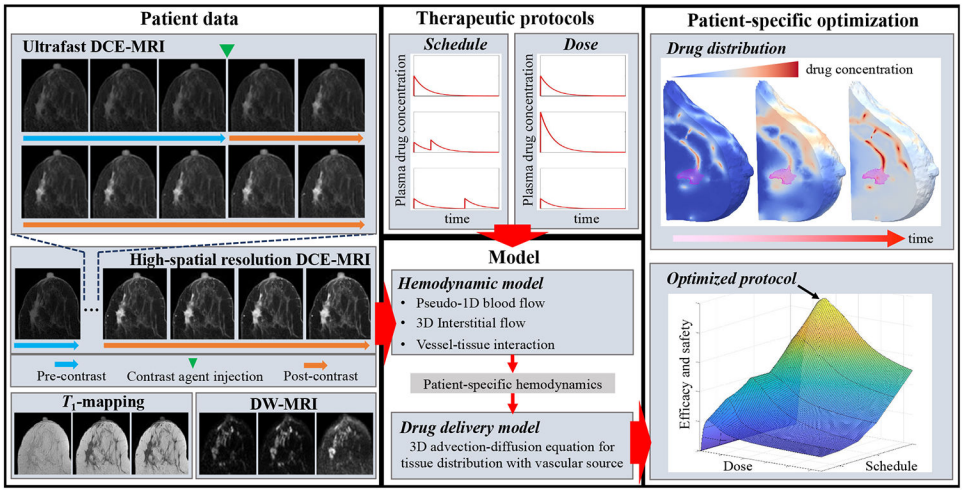

Fig. 1.

Flow chart of the image processing and simulation framework. The first panel on the left, “Patient data”, displays the unprocessed MRI images, including ultra-fast DCE-MRI, high-spatial resolution DCE-MRI, variable flip angle data for T_1-mapping, and DW-MRI. For the DCE series, the cyan and orange arrows represent the pre-and post-contrast scans, respectively. Imaging data are then processed and imported into the model; i.e., the panel labeled “Model”, which consist of the hemodynamic and drug delivery models to estimate patient-specific characteristics. These data are coupled with specific protocols, as shown in the panel “Therapeutic protocols”, to estimate treatment-specific drug distribution on an individual patient basis. As presented in the panel labeled, “Patient-specific optimization”, the spatiotemporal changes in drug distribution are computed during the whole treatment cycle for a range of treatment protocols. The last step is to determine the optimal treatment protocol that provides the best performance regarding therapeutic efficacy and toxicity.

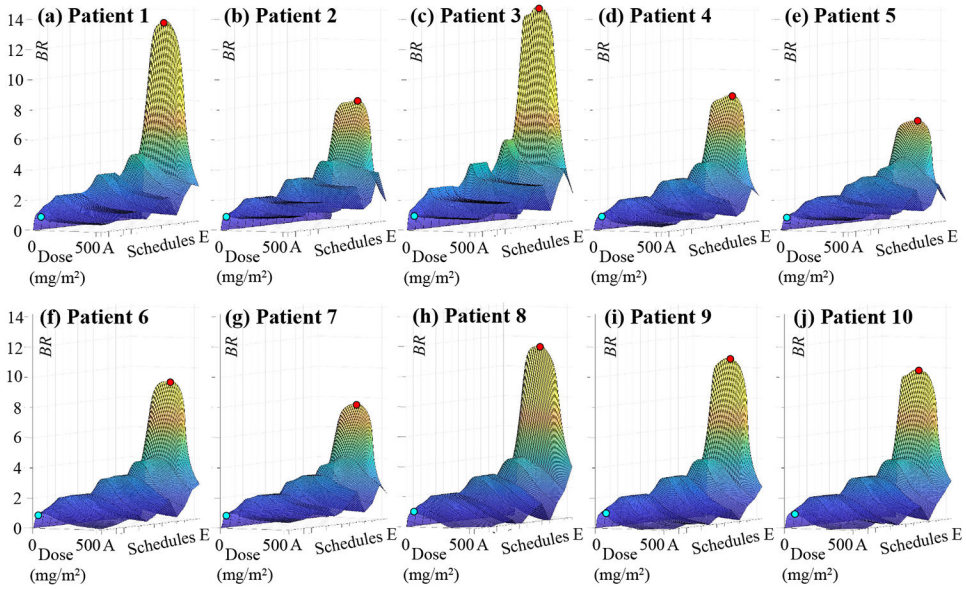

Fig 2.

Improvement in treatment efficacy and safety provided by the optimized treatment protocols. Panels (**a – j**) present surface plots indicating the *BR* achieved with each candidate treatment protocol with respect to the standard regimen for each patient. The *x*-*y* plane spans the space of potential treatment protocols, where the *x*-axis represents the total dose given and the *y*-axis refers to the 14 injection schedules investigated in this work. In each surface plot, the altitude (i.e., height along the *z*-axis) and color indicate the performance of the tested protocol, where a higher *BR* indicates better performance. The standard regimen and optimal schedule are labeled as cyan and red circles on each surface plot, respectively. Overall, schedule E with a patient-specific optimized dose leads to the best *BR* for all patients in this cohort.

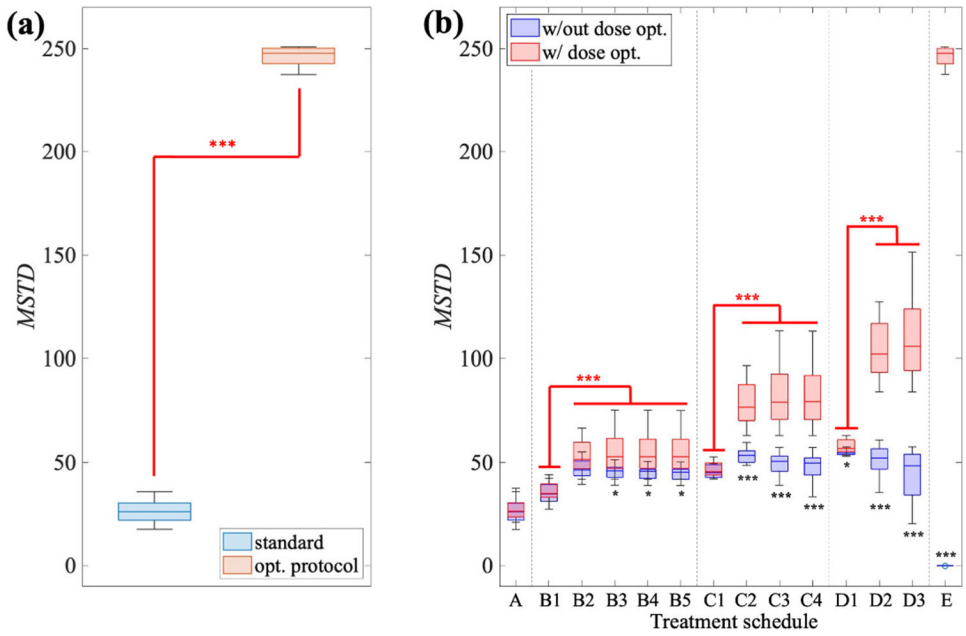

Fig 3.

Statistical comparisons of the different treatment protocols. Panel (**a**) compares the *MSTD*s between the standard (blue) and the patient-specific optimal protocol (red) across the cohort. In each boxplot, the median (central line), interquartile range (box) and the entire range without outliers (black whisker) are shown. Overall, the *MSTD*s achieved by the patient-specific optimal protocols are significantly higher than the ones achieved by the standard protocol for all patients. Panel (**b**) presents the *MSTD* achieved by each treatment schedule with the standard total dose (i.e., 60 mg^2/m^2 BSA; blue) and the individually optimized total dose (red) across the cohort. The Wilcoxon rank-sum test is performed for all statistical comparisons involved in this figure. The '*' and '***' indicate statistical significance at the $P < 0.05$ and $P < 0.001$ levels, respectively.

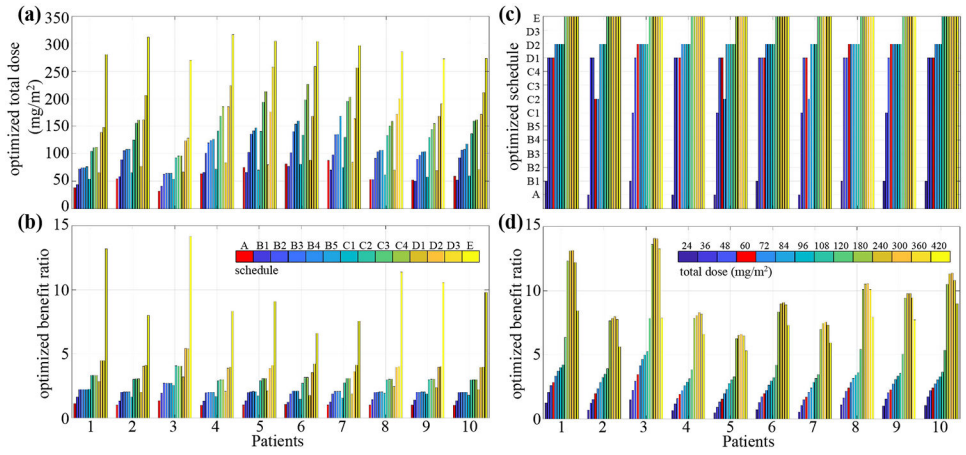

Fig 4.

Personal optimization of therapeutic protocols. Panels (**a-b**) depict different therapeutic schedules yield different optimized total doses and different optimized benefit ratios (BR). Given the candidate schedules A – E (with red representing the standard schedule), we find the optimized total dose for each patient (**panel a**) and the corresponding optimized *BR* (**panel b**). Each group of bars in the panel **(a)** indicates that each administration schedule yields a different optimal total dose for each patient; specifically, schedules with higher injection frequency tend to require higher optimal total dose. Each group of bars in panel **(b)** indicates that the optimal benefit ratio is always achieved by schedule E for each patient. Bars with the same color in panel **(a)** show, given a specific schedule, the optimal dose varies across patients. Bars with the same color in panel **(b)** show, given a specific schedule, the optimal benefit varies across patients. Panels (d-c) depict different total doses yield different optimized schedules and different optimized benefit ratios. Given the candidate total doses, 24 – 420 mg/m^2 (with red representing the standard dose), we find the optimal administration schedule for each patient (**panel c**) and the corresponding optimized *BR* (**panel d**). Each group of bars in panel **(c)** indicates that each total dose yields a different optimal schedule for each patient. Each group of bars in panel **(d)** indicates that the optimal benefit ratio is always achieved by a total dose within the range of 180 – 360 mg/m^2. Bars with the same color in panel **(c)** show, given a specific total dose, the optimal schedule can vary across patients. Bars with the same color in panel **(d)** show, given a specific dose, the optimal benefit varies across patients.

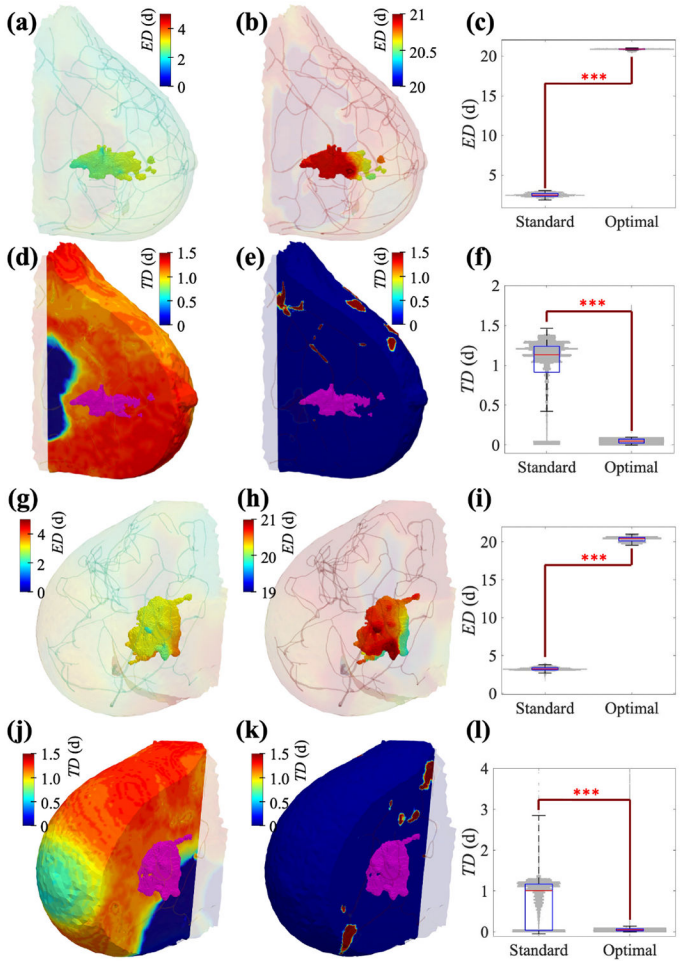

Fig 5.

ED and *TD* maps produced by the standard and optimal treatment protocols for Patient 1 (**a-f**) and Patient 2 (**g-l**). Panels (**a**) and (**b**) show the *ED* maps throughout the breast (transparent volume) as well as the tumor surface (solid volume) for the standard and optimized treatment protocols, respectively. Panels (**d**) and (**e**) show the *TD* maps throughout the non-tumor breast tissue (solid, color-coded volume) for the standard and optimized treatment protocols, respectively, with the tumors shown as solid, magenta volumes. Panels (**c**) and (**f**) respectively show boxplots of the distribution of the *ED* within the tumor and the *TD* outside the tumor for both the standard and optimized regimens. In these panels, the distributions of *ED* and *TD* values are shown as gray areas, while the median (red line), interquartile range (blue box) and entire range without outliers (black whisker) define the boxplot. The symbol '***' indicates statistical significance at the $P < 0.001$ level by the Wilcoxon rank-sum test. Panels (**g-l**) display the corresponding data for Patient 2. Compared to the standard treatment protocol, the optimized protocol leads to a significantly higher *ED* within tumor and a significantly lower *TD* in the healthy tissue. Therefore, the optimized protocol contributes to enhance treatment efficacy in the tumor while limiting toxicity to the rest of the organ.

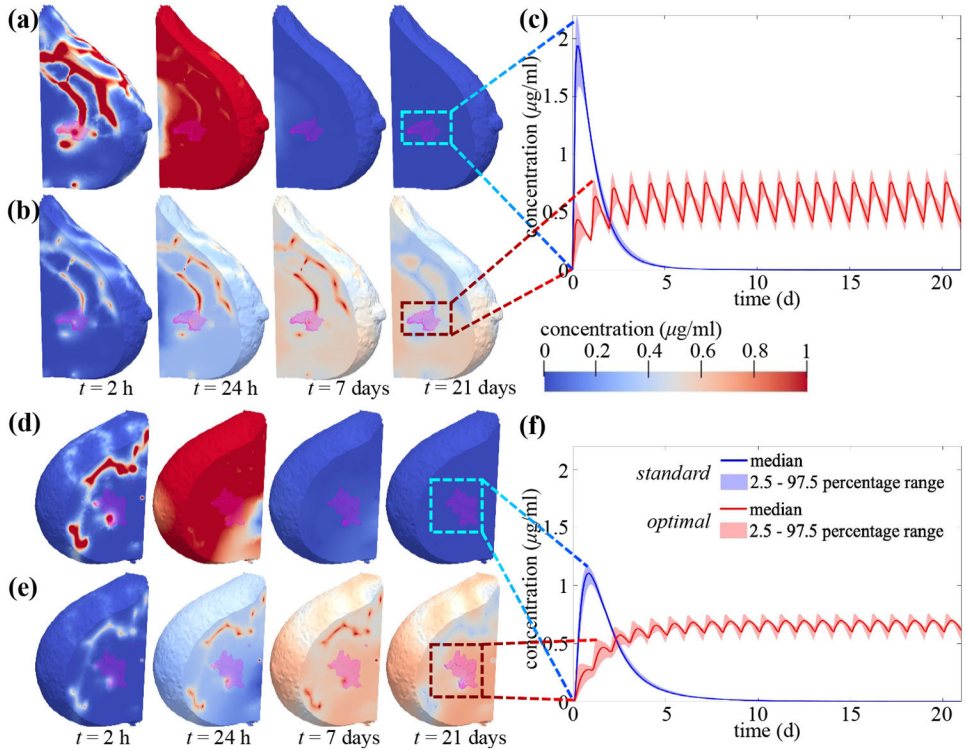

Fig 6.

Drug distribution over time for Patient 1 (**a-c**) and Patient 2 (**d-f**). Panels (**a**) and (**b**) show the simulated 3D drug distribution dynamics throughout the breast (solid volume) and tumor (purple transparent volume) resulting from the standard and optimal treatment protocols, respectively, for Patient 1. Within each row, the columns (from left to right) indicate the drug distributions at 2 h, 24 h, 7 days, 21 days post-injection, respectively. Additionally, the median (and range) of drug concentration time courses sampled at the equivalent voxels within the tumor is presented in panel (**c**), where the standard and optimal protocols are shown as blue and red, respectively. Panels (**d-f**) display the corresponding data for Patient 2. As compared to the standard treatment protocol, the optimized protocol leads to a more consistent concentration of drug across the therapeutic cycle. Qualitatively, Patient 1 has a faster drug uptake and higher peak concentration, as well as a larger range of concentration oscillation in the optimal protocol.

TABLE I.

Model Geometry, Variables, and Parameters

Quantities		Definition (units)
Geometry	Ω_t	Interstitial tissue domain (−)
	Ω_v	Vascular region (−)
	Ω_{tumor}	Tumorous region (−)
	Λ	Vascular centerlines (−)
	l	Position along vessels (cm)
	$\boldsymbol{x}$	Coordinate in interstitial tissue (cm×cm×cm)
	$\boldsymbol{n}$	Unit normal at vascular surface (cm×cm×cm)
Parameter	μ	Blood dynamic viscosity (g/(cm s))
	$R(l)$	Vessel radius (cm)
	$L_p(l)$	Vascular hydraulic conductivity (cm^2 s/g)
	$\kappa(\boldsymbol{x})$	Tissue hydraulic conductivity (cm^3 s/g)
	$D(\boldsymbol{x})$	Interstitial diffusivity of drug (cm^2/s)
	$^{\mathrm{P}}(\boldsymbol{x})$	Apparent vascular permeability (ml/(cm^2 s))
Variable	$p_v(l)$	Blood pressure (g/(cm s^2))
	$Q_v(l)$	Blood flow rate (cm^3/s)
	$p_t(\boldsymbol{x})$	Interstitial pressure (g/(cm s^2))
	$\boldsymbol{u}_t(\boldsymbol{x})$	Interstitial flow velocity (cm/s)
	$q_e(l)$, $q_e(\boldsymbol{x})$	Net efflux across vessel wall (cm/s)
	$C_p(t, l)$	Plasma concentration of drug (μg/ml)
	$C_t(t, \boldsymbol{x})$	Tissue concentration of drug (μg/ml)
	$\boldsymbol{J}(t, \boldsymbol{x})$	Efflux of drug from vessels (μg/(cm^2 s))

TABLE II.

Candidate Treatment Protocols

Sch.	# of inj	Dose fraction per inj	Injection times
A	1	1	day 1
B1	2	1/2	day 1, day 2
B2			day 1, day 4
B3			day 1, day 6
B4			day 1, day 8
B5			day 1, day 11
C1	3	1/3	day 1, day 2, day 3
C2			day 1, day 4, day 7
C3			day 1, day 6, day 10
C4			day 1, day 8, day 15
D1	4	1/4	day 1, day 2, day 3, day 4
D2			day 1, day 4, day 7, day 10
D3			day 1, day 6, day 11, day 16
E	21	1/21	every day